Check for updates

Hydrogen induced interface engineering in Fe₂O₃–TiO₂ heterostructures for efficient charge separation for solar-driven water oxidation in photoelectrochemical cells†

Aadesh P. Singh, [ID] *[a] Richard Baochang Wang, [ID] [b] Camilla Tossi, [ID] [a] Ilkka Tittonen, [ID] [a] Björn Wickman [ID] [b] and Anders Hellman [ID] *[b]

Semiconductor heterostructure junctions are known to improve the water oxidation performance in photoelectrochemical (PEC) cells. Depending on the semiconductor materials involved, different kinds of junctions can appear, for instance, type II band alignment where the conduction and valence bands of the semiconductor materials are staggered with respect to each other. This band alignment allows for a charge separation of the photogenerated electron–hole pairs, where the holes will go from low-to-high valance band levels and *vice versa* for the electrons. For this reason, interface engineering has attracted intensive attention in recent years. In this work, a simplified model of the Fe₂O₃–TiO₂ heterostructure was investigated *via* first-principles calculations. The results show that Fe₂O₃–TiO₂ produces a type I band alignment in the heterojunction, which is detrimental to the water oxidation reaction. However, the results also show that interstitial hydrogens are energetically allowed in TiO₂ and that they introduce states above the valance band, which can assist in the transfer of holes through the TiO₂ layer. In response, well-defined planar Fe₂O₃–TiO₂ heterostructures were manufactured, and measurements confirm the formation of a type I band alignment in the case of Fe₂O₃–TiO₂, with very low photocurrent density as a result. However, once TiO₂ was subjected to hydrogen treatment, there was a nine times higher photocurrent density at 1.50 V *vs.* the reversible hydrogen electrode under 1 sun illumination as compared to the original heterostructured photoanode. *Via* optical absorption, XPS analysis, and (photo)electrochemical measurements, it is clear that hydrogen treated TiO₂ results in a type II band alignment in the Fe₂O₃–H:TiO₂ heterostructure. This work is an example of how hydrogen doping in TiO₂ can tailor the band alignment in TiO₂–Fe₂O₃ heterostructures. As such, it provides valuable insights for the further development of similar material combinations.

1. Introduction

Solar energy-assisted splitting of water into its constituents, hydrogen and oxygen, in a photoelectrochemical (PEC) cell, represents a promising route to convert solar energy into more useful chemical fuels.[1,2] The water reduction process can produce hydrogen, where the required electrons can be generated *via* the water oxidation reaction at the surface of a photoanode through PEC reactions. However, the water oxidation reaction is a demanding electrochemical process, requiring an oxidatively robust and yet inexpensive semiconducting material as the photoanode.[3] Despite tremendous efforts, developing a highly active photoanode for water oxidation at low cost remains a significant challenge. After the first report on water splitting by Fujishima and Honda,[4] titanium dioxide (TiO₂) in its anatase phase has been extensively studied in solar-driven photocatalytic processes.[5–7] However, for practical applications, the large bandgap of TiO₂ (~3.2 eV) requires solar radiation with wavelength below 388 nm to create an electron–hole pair; thereby, limiting the overall efficiency of TiO₂ when illuminated under real Sun conditions.[8,9] Another material of high interest for PEC water splitting is hematite (α-Fe₂O₃), due to its suitable band gap (2.1 eV), high stability over a wide range of pH and potentials, and low material cost.[10,11] In spite of these various advantages, the solar-to-hydrogen conversion efficiency of α-Fe₂O₃ falls well below the theoretical maximum value (≈12.9%) due to a number of factors such as (i) bulk charge recombination, (ii) interfacial carrier trapping and

ᵃDepartment of Electronics and Nanoengineering, School of Electrical Engineering, Aalto University, P.O. Box 13500, 00076 Aalto, Finland. E-mail: aadesh.singh@aalto.fi

ᵇDivision of Chemical Physics, Department of Physics, Chalmers University of Technology, SE-412 96 Göteborg, Sweden. E-mail: anders.hellman@chalmers.se; Tel: +46 31 772 5611

recombination, (iii) surface trapping and recombination, and (iv) improper band positions for unassisted water splitting[12] (see Fig. S1† for further information).

To address the issues with solely α-Fe$_2$O$_3$ and TiO$_2$ based oxide semiconductors and design a photoanode for PEC water oxidation with high solar-to-hydrogen conversion efficiency, the heterostructure of these two semiconductors has been recognized as an attractive candidate to enhance the photocurrents and lower the onset potential.[13,14] The combined properties of α-Fe$_2$O$_3$ and TiO$_2$ allow the heterostructures to absorb a wider range of photons, thanks to the relatively narrow band gap of α-Fe$_2$O$_3$.[15] Also, the formation of heterostructures between α-Fe$_2$O$_3$ and TiO$_2$ can allow band structure engineering to manipulate surface/interface properties for charge transfer/separation, thereby enhancing the water oxidation performance.[16] In particular, the valence and conduction band alignment mechanisms at the interface are crucial for the separation of photogenerated charge carriers.[17] In both oxide semiconductors, the Fermi levels depend on the concentrations of the conduction electrons and hence on the oxygen vacancy concentrations. By appropriate adjustments of the Fermi levels *via* defect concentration, the valence band edge in the bulk of the semiconductor may be brought to a common equilibrium. Using the available data[18] of the electron affinities for Fe$_2$O$_3$ (4.71 eV) and TiO$_2$ (4.33 eV), together with the generally accepted model of heterojunctions, the discontinuity at the conduction bands (CB) is estimated to be 0.38 eV while that for the valence bands (VB) is estimated to be 0.42 eV. Owing to the mutual positions of Fe$_2$O$_3$ and TiO$_2$ conduction band edges, photogenerated electrons in TiO$_2$ can be easily transferred to Fe$_2$O$_3$ and injected into the Indium Tin Oxide (ITO) substrate, and subsequently can migrate through the external electric circuit to reduce water at the cathode, thus suppressing detrimental recombination effects (Fig. 1a). On the other hand, the VB offset at the interface by 0.42 eV act as an energy barrier that blocks the hole transfer from the α-Fe$_2$O$_3$ to the TiO$_2$ layer and prevents the water oxidation reaction on the surface of TiO$_2$ (Fig. 1a). This means the heterostructure between α-Fe$_2$O$_3$ and TiO$_2$ forms a type I band alignment at the semiconductors' interface, and the hole transport from α-Fe$_2$O$_3$ to TiO$_2$ is energetically impeded, as depicted in Fig. 1a and b.

However, in the case of a thin pours TiO$_2$ layer (<100 nm) over Fe$_2$O$_3$ and at applied anodic potential, the depletion region and upward band bending in TiO$_2$ at Fe$_2$O$_3$–TiO$_2$ nano-heterostructure in contact with the electrolyte may extend into the α-Fe$_2$O$_3$. This high band bending in the thin TiO$_2$ overlayer, under the influence of anodic potential, can provide a channel to transfer the photogenerated holes from Fe$_2$O$_3$ to TiO$_2$ where they participate in the water oxidation reaction, thereby improving the water oxidation performance of the Fe$_2$O$_3$–TiO$_2$ photoanode. Barreca *et al.*[15] reported that the use of external potential could transfer of photogenerated holes from porous hematite to TiO$_2$ layers that can improve the PEC response under simulated light. However, in the case of thick and dense TiO$_2$ layer over α-Fe$_2$O$_3$, the mismatched band alignment can hinder the charge transfer process at Fe$_2$O$_3$–TiO$_2$ heterostructure, thereby constitute the limiting factor in PEC applications. Therefore, for swift transfer of photogenerated holes from VB of α-Fe$_2$O$_3$ to the VB of TiO$_2$, band edge and band gap tailoring in TiO$_2$ are required to form a type II band alignment at the Fe$_2$O$_3$–TiO$_2$ heterostructure interface. In our previous study,[8,9,17] we demonstrated that a high temperature hydrogen treatment in TiO$_2$ under partial pressure can modify the structural, optical, and electrical properties and significantly improve the photocatalytic and photoelectrochemical performance. An upshift of the valence band of TiO$_2$ was achieved after the high temperature hydrogen treatment at partial pressure that was useful for band edge engineering at TiO$_2$–BiVO$_4$ heterostructure. However, a downshift of valance band maximum (VBM) was also obtained when TiO$_2$ thin films were grown *in situ* in hydrogen plasma.[19]

In this study, first-principles calculations on a model Fe$_2$O$_3$–TiO$_2$ heterostructure show that the strain at the interface shifts the valance and conduction band positions and affects the bandgap of the TiO$_2$ layer. Furthermore, the calculations show that neutral and positive charged H interstitials are energetically preferred under hydrogen treatment conditions. These interstitials introduce states in the bandgap of TiO$_2$, which can assist in the transfer of holes through the TiO$_2$ layer. To challenge the theoretical predictions, well-defined planar Fe$_2$O$_3$–TiO$_2$ heterostructures were manufactured. The experimental results show that Fe$_2$O$_3$–TiO$_2$ initially forms a type I band
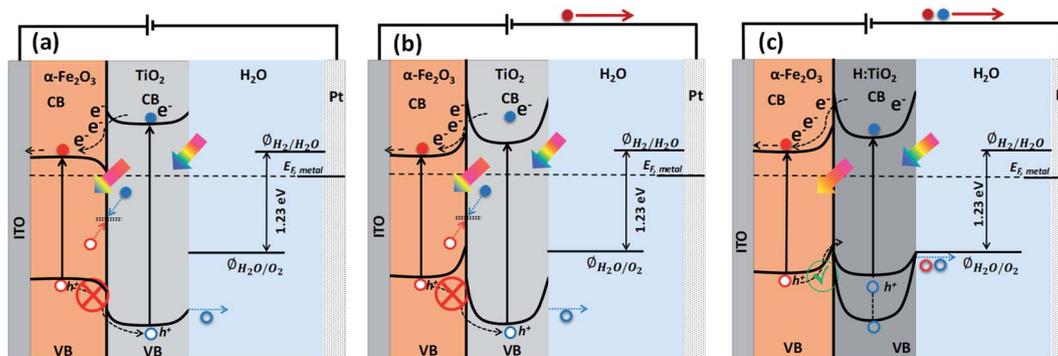

Fig. 1 Approximate energy band diagram and charge transfer mechanism of (a) Fe$_2$O$_3$–TiO$_2$ photoanode without external applied anodic potential, (b) Fe$_2$O$_3$–TiO$_2$ photoanode with external applied anodic potential and (c) Fe$_2$O$_3$–H:TiO$_2$ photoanode with external applied anodic potential.

alignment, prohibiting the transfer of holes through TiO_2. However, after hydrogen treatment, the Fe_2O_3–H:TiO_2 heterostructure seems to form a type II band alignment; thus, hole transfer becomes possible, leading to an enhanced PEC response.

2.   Experimental section

2.1   Preparation of α-Fe_2O_3 thin films

The ultra-thin hematite films were prepared onto indium-doped tin oxide (SnO_2:In, ITO, PGO GmbH, sheet resistance < 20 Ω sq^{-1}) substrate by using physical vapor deposition technique, followed by annealing of Fe coated ITO substrate in air atmosphere.[20] Briefly, all the substrates were cleaned by using soap solution, acetone, and deionized water followed by ultra-sonication in isopropanol for 5 minutes and finally with oxygen plasma for two minutes. Before deposition, 1/3 area (5 mm × 10 mm) of the substrate was covered with a thermal tape for making the electrical contact later for PEC measurements. To fabricate the ultra-thin hematite film (approximately 25 nm), a 10 nm thick Fe films were deposited on ITO substrate by physical vapor deposition (PVD 225, Kurt J. Lesker, base pressure < 5 × 10^{-7} mbar) and annealed in air atmosphere at 350 °C for 8 h with a heating rate of 4 °C min^{-1}. The thickness of the Fe film was measured *in situ* during deposition using a quartz-crystal microbalance monitor integrated in PVD system. After annealing, the samples were allowed to cool down to room temperature naturally.

2.2   Preparation of Fe_2O_3–TiO_2 and Fe_2O_3–H:TiO_2 heterostructures

Thin films of TiO_2 were deposited onto ITO substrates and also on hematite coated ITO substrate by sol–gel technique.[6] In short, a transparent gel solution of titanium dioxide was prepared by mixing 3 ml titanium tetra-isopropoxide (TTIP, 97% pure) in 20 ml ethanol in the presence of diethanolamine. The solution was stirred for 4 h at room temperature to enhance the reaction rate between diethanolamine and TTIP, and finally, it was converted into a gel. This gel solution was applied on α-Fe_2O_3/ITO substrate and uniformly coated with the help of a spin coating unit at 3000 rpm for 1 minute. A thin layer of TiO_2 was achieved by the deposition of prepared gel over the α-Fe_2O_3/ITO substrates. After deposition, the prepared TiO_2–Fe_2O_3 heterostructure was allowed to dry for 10 min at 80 °C and further annealed at 350 °C for 4 h. The hydrogen treatment was carried out by annealing the Fe_2O_3–TiO_2 heterostructures at 300 °C in 4% H_2 in Ar at atmospheric pressure for 6 h. We also prepared a hydrogen doped TiO_2 thin film photoanode under the same annealing conditions to see the effect of hydrogen doping individually on optical, electrical, and PEC properties.

2.3   Material characterization

The chemical phase of the prepared samples was determined by using a confocal Raman microscope (alpha300 R; WITec) with a 488 nm laser pulse as an excitation source. The surface morphology of the bare and TiO_2 coated α-Fe_2O_3 samples was examined by field emission scanning electron microscope (FE-SEM) using a Zeiss Supra 60 VP microscope operated at an acceleration voltage of 10 kV. The optical absorption of all the samples was measured with the help of a Cary 5000 spectrophotometer (Varian). X-ray photoelectron spectroscopy (XPS) spectra were acquired in a PerkinElmer Phi 5500 setup (base pressure < 10^{-10} mbar) using AlK$_\alpha$ radiation of 1.4866 keV. The XPS spectra were shifted using the Fe(2p$_{3/2}$) peak corresponding to 710.9 eV as a reference.

2.4   Photoelectrochemical measurements

For electrochemical measurements, thin films of α-Fe_2O_3, TiO_2, H:TiO_2, Fe_2O_3–TiO_2 and Fe_2O_3–H:TiO_2 heterojunctions were converted into the photoelectrodes with an active surface area of about 0.50 cm^2. All the (photo)electrochemical measurements, current–voltage (*I*–*V*), capacitance–voltage (*C*–*V*), and electrochemical impedance spectroscopy (EIS), were conducted in a three-electrode configuration using a H-type PEC cell made of glass and fitted with a flat optical quartz window containing 0.1 M NaOH as electrolyte (pH = 12.9). The PEC cell was controlled by using the Gamry Ref. 600 potentiostat and a solar simulator (SKU SS150, Sciencetech Inc.) with an output intensity of 100 mW cm^{-2} as an illumination source. Here, the prepared photoelectrodes were used as a working electrode, Pt wire as a counter electrode, and Ag/AgCl as a reference electrode. For better representation of our results, the Ag/AgCl reference potential was converted into the reversible hydrogen electrode (RHE) potential by using the following formula: $V_{RHE} = V_{Ag/AgCl} + 0.059pH + V^o_{Ag/AgCl}$, where $V^o_{Ag/AgCl}$ is the standard potential of Ag/AgCl at 25 °C (0.1976 V *vs.* the standard hydrogen electrode, SHE). The cyclic voltammetry sweep scans in the potential range between 0 and 2.0 V_{RHE} at a scan rate of 10 mV s^{-1} were performed to obtain the *I*–*V* characteristics under dark and illumination. The photocurrent density (J_{ph}) has been calculated by subtracting the dark current from the current measured under illumination and devised by the geometrical area of the photoanode. Electrochemical impedance spectroscopic (EIS) measurements under illumination were carried out in the frequency range 10^5 and 0.1 Hz at applied potentials between 1.23 V_{RHE}. Nyquist plots obtained under illumination were fitted using the software EIS spectrum analyzer. Mott–Schottky analysis was performed at an applied frequency of 1 kHz in the dark condition in a potential window between 0 and 1.5 V_{RHE}. The obtained Mott–Schottky curves ($1/C^2$ *versus* V_{RHE}) were used to determine the donor density (N_D) and flat band potential (V_{fb}) by using the Mott–Schottky equation: $C^{-2} = (2/q\varepsilon_o\varepsilon_s N_D)[V - V_{fb} - kT/q]$, where ε_o is the permittivity of the vacuum, ε_s is the dielectric constant of the hematite, q is the electronic charge, and kT/q is the thermal voltage (26 meV at room temperature). The donor density was calculated using the equation, $N_D = 2/(\varepsilon_o\varepsilon_s q)[d(1/C^2)/dV]^{-1}$, from the slope of the linear region, between 0.6 and 1.0 V_{RHE}, of Mott–Schottky plots.

2.5   Computational methods

The first-principles calculations were performed using density functional theory (DFT) as implemented in the VASP

package.[21–23] The interaction between the valance electrons and the core follows the projector augmented wave (PAW) method.[24] PAW potentials with the valence states 1s for H, 2s and 2p for O, 3d and 4s for Fe, and 3d and 4s for Ti have been employed. A plane wave basis with a kinetic energy cut-off 700 eV was used. To improve convergence, a Gaussian smearing broadening of the Fermi surface of 0.1 eV was employed. The exchange–correlation (XC) interaction was treated at the level of the generalized gradient approximation (GGA) using the XC-functional of Perdew, Burke, and Ernzerhof (PBE).[25] In the DFT+U calculations, the rotationally-invariant scheme proposed by Dudarev et al.[26] and a $U - J = 4.3$ eV on Fe atom and $U - J = 5.2$ eV on Ti atom are employed in all our calculations.[27,28] The HSE06 method, as implemented in VASP, was employed to study H defects in anatase TiO$_2$.[29,30] A kinetic cut-off of 600 eV was applied in all calculations. The interface system is composed of a six-layer thick Fe$_2$O$_3$ with a (0001) termination of p(2 × 2), that is joined with a four-layer thick anatase TiO$_2$ with a (101) termination of p(1 × 2). Owing to the lattice mismatch between Fe$_2$O$_3$ and TiO$_2$, the interface will introduce strain to the system. Here the lattice cell ($a = b = 10.17$ Å, $a = 120°$) of Fe$_2$O$_3$ (0001) surface is kept fixed, which implies a strain to the original lattice cell ($a = 11.35$ Å, $b = 10.23$ Å, alpha = 111.69°) of the TiO$_2$ (101) surface. The strain amounts to 10% compression strain on the a-axis and 0.6% compression strain to the b-axis, and an increase of the angle by 7.4%. During the relaxation of the interface system, the anatase TiO$_2$ reconstructs to amorphous TiO$_2$ (a-TiO$_2$). Here, the term amorphous is used to indicate that the reconstructed TiO$_2$ in the interface model can not be identified with any known phase (rutile, anatase, brookite, etc.) of TiO$_2$. However, it should be noted that due to the periodic conditions, this phase should not be considered as genuinely amorphous TiO$_2$. Defect calculations were carried out in a $2\sqrt{2} \times 2\sqrt{2} \times 1$ (96 atoms) supercell of anatase TiO$_2$, with a Γ-centered $1 \times 1 \times 1$ k-point sampling. The effect of higher concentrations of defects is modeled by a $\sqrt{2} \times \sqrt{2} \times 1$ (24 atoms) supercell and a $1 \times 1 \times 1$ (12 atoms) unit cell, using a $3 \times 3 \times 1$ Monkhorst–Pack (MP) sampling.[31] All geometries were relaxed until the maximum force was less than 0.05 eV Å^{-1}. The relative stability of the various defects in charged and/or neutral states is determined by the formation energy,

$$\Delta E_f = E_t(D^q) - E_t(TiO_2) - \Delta n_O \mu_O - \Delta n_H \mu_H + qE_F + E_{corr}, \quad (1)$$

where $E_t(D^q)$ is the total energy of the supercell containing a defect D in charge state q and $E_t(TiO_2)$ is the total energy of a perfect crystal in the same supercell. Δn_O and Δn_H are the number of O atom and H atom changed in the defective supercell with respect to the perfect one. μ_O and μ_H are the chemical potential of O atom and H atom. E_F and E_{corr} refer to the energy of the Fermi level and the Madelung corrections for the electrostatic interaction between the homogeneous background charge and charged defects. The chemical potential of the O atom is selected to satisfy the stability condition of TiO$_2$.

In the extreme O-rich limit, the μ_O is set to $\frac{1}{2}E(O_2)$, where $E(O_2)$

is the calculated total energy of isolated O$_2$ molecule. In the extreme O-poor limit, μ_O corresponds to the formation of Ti$_2$O$_3$, which has a relationship of μ_O(O-poor) $= \mu_O$(O-rich) $- 3.97$ eV calculated by HSE06. μ_H is selected as one half of the total energy of isolated H$_2$ molecule, $\frac{1}{2}E(H_2)$.

3. Results

3.1 Simulation results

The valence band offset (VBO) at the interface of Fe$_2$O$_3$ and a-TiO$_2$ was calculated through the reference potential method originally introduced by Kleinman[32,33] where the reference potential use the macroscopically averaged electrostatic potential.[34] The calculated results are shown in Fig. 2. The VBO for the individual system, Fe$_2$O$_3$ (0001) and a-TiO$_2$ thin film, were also calculated and are shown in the ESI (Fig. S2).† The blue curve in Fig. 2 refers to the electrostatic potential calculated using PBE+U method. The valence band edges of Fe$_2$O$_3$ and a-TiO$_2$ were determined with respect to the macroscopically averaged electrostatic by performing calculations on the separated systems. The values of Fermi energy were calculated to 3.88 eV and 0.87 eV for Fe$_2$O$_3$ (0001) and a-TiO$_2$ thin film, respectively. The macroscopically averaged electrostatic potential was calculated by,
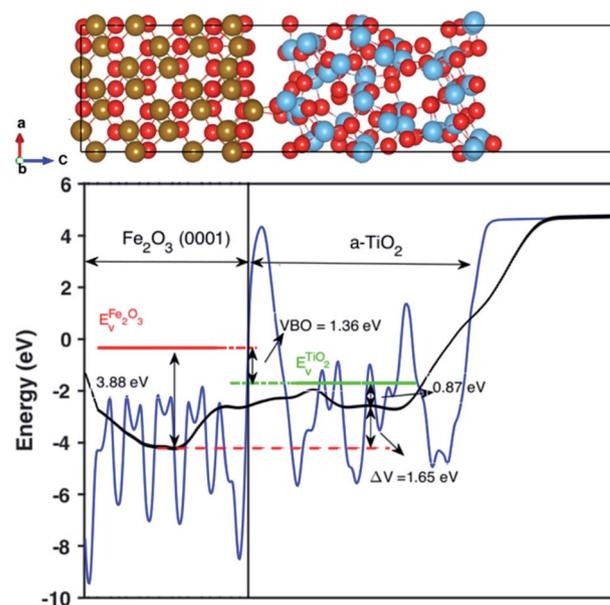

Fig. 2 Up panel is the relaxed structures from the PEB + U calculation for the Fe$_2$O$_3$ and amorphous TiO$_2$ interface. Bottom panel is the calculated valence band offset (VBO) of the interface with PBE+U methods. The black line is the calculated macroscopically averaged electrostatic potential and the blue line is the electrostatic potential at the interface averaged along the thickness (c-axis) of the interface. The red line is the position of VBM of Fe$_2$O$_3$ and the green line is the position of VBM of bulk TiO$_2$ with respect to vacuum level. The electrostatic potential across the interface is $\Delta V = 1.65$ eV and the calculated VBO at the interface is 1.36 eV. The VBO of the joint interface is slightly larger than that of separated systems by 0.18 eV that indicating the creation of an interface dipole or double layers.[37]

$$V'(z) = \int dz' \int dz'' w_{l_1}(z - z') w_{l_2}(z' - z'') V'(z''), \qquad (2)$$

where $w_l(z - z') = \frac{1}{l} \Theta\left(\frac{l}{2} - z\right)$, Θ is the unit-step function, l_1 and l_2 are in the order of the (strained) thickness of hematite (0001) and amorphous TiO_2 thin film along z, respectively.

$$\Theta = \begin{cases} 0, z < 0. \\ 1, z \geq 0. \end{cases} \qquad (3)$$

where $V'(z)$ is the xy-plane averaged electrostatic potential and d_1 and d_2 are the inter-planar distances along the z direction (normal to the interface).[35,36]

The calculated $V'(z)$ is the black line in Fig. 2. The VBO was calculated via,

$$VBO = \Delta E_v + \Delta V. \qquad (4)$$

The calculated VBO for the individual system is -1.18 eV using DFT+U, which agrees well with the experimental observations ($\sim$0.5 eV).[38] However, the calculated VBO at the interface is around 1.36 eV, with the valence band edge of TiO_2 sitting below the Fe_2O_3, which is 0.18 eV higher than the separated systems indicating an interface dipole or double layer were created at the interface. The electrostatic potential across the interface is $\Delta V = 1.65$ eV.

We further studied H defects and O vacancy in anatase TiO_2, including their formation energy and electronic structure. The formation energy is calculated using eqn (1), and the results are shown in Fig. 3a, which corresponds to the results from the modeled supercell of 96 atoms. It is clearly shown that the positively charged H interstitial is the most favorable (with negative formation energy) defect when the Fermi energy is located above the valence band edge and below 2.9 eV, while the H interstitial becomes stable when E_f is larger than 2.9 eV (see Fig. 3). The formation energy of H interstitial is 0.04 eV. In contrast, O vacancies and substitutional H are less energetically favorable.

Next, we have studied the formation energies of different concentrations of defects in anatase TiO_2 using different supercells, and the results are shown in Fig. 3b. Here, the formation energy plot is shown for O-rich conditions and the Fermi energy is set to 3.0 eV. As seen from Fig. 3b, the two most stable defect configurations are neutral and positively charged H interstitials, H_i, where the positively charged H interstitial is the most favorable defect at high concentrations. The neutral H interstitial is the second state configuration when H concentration larger than 4 at%. The other defects are less stable as their formation energies are very high (larger than 3 eV). At high concentration (8 at%), the substitutional H_s becomes more stable than O vacancies. Interestingly, under O-poor conditions,
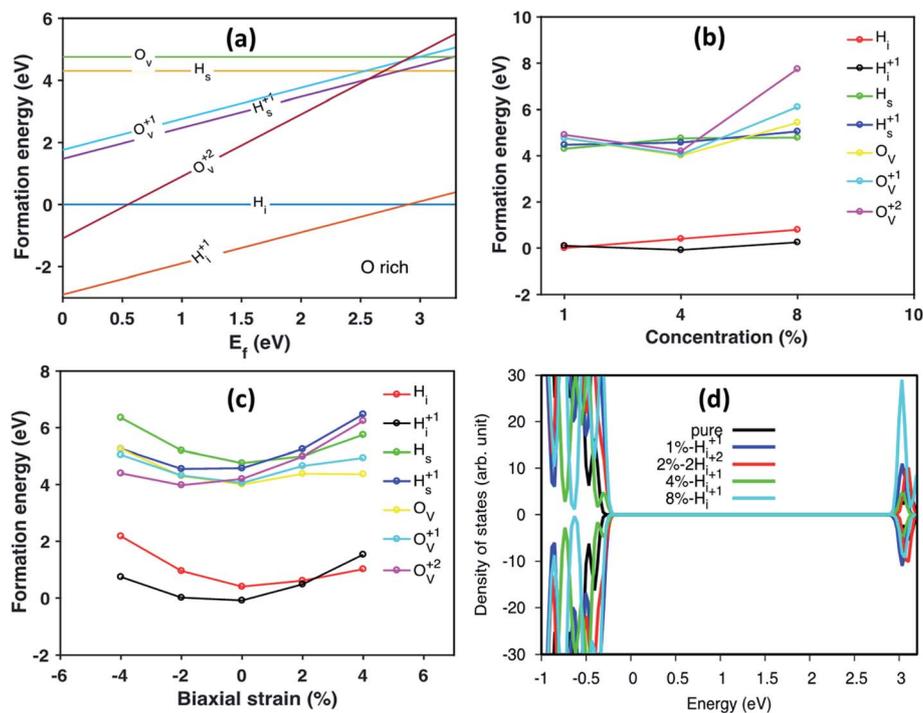

Fig. 3 (a) The formation energy of different charged defects in anatase TiO_2 under oxygen rich conditions corresponding to the current experiment condition. The Madelung corrections, E_{corr} is taken to be 0.1 eV in all our calculations. The x-axis is the Fermi energy level of anatase TiO_2. O_v denotes the oxygen vacancy and can neutral (O_v), +1 positively charged (O_v^{1+}) or +2 positively charged (O_v^{2+}). H_i is the interstitial H defect and H_s is the substitutional hydrogen defect. (b) The calculated formation energy of various defects in anatase varying with the defect concentration under O-rich condition. The Fermi energy is set to $E_f = 3.0$ eV. (c) The calculated formation energy of different charged/neutral defects under biaxial strain from -4% to $+4\%$ under O-rich condition. The Fermi energy is set to $E_f = 3.0$ eV. (d) The calculated density of states (DOS) of pure anatase and anatase with H_i^+ in different concentrations. The energy was aligned by the 1s state of O atom far away from the defect.

the H_s is as stable as the H_i (the formation energy plot is shown in Fig. S3†).

When constructing the interface, a strain is induced automatically due to the lattice mismatch. Therefore, we also studied the stain effects on defect configurations for defect concentration of 4 at%. The calculated formation energy of different defects under biaxial strain is shown in Fig. 3c. It is interesting to notice that under biaxial tensile strain, the stable defect configuration changes to H_i. Under compressive strain, positively charged H_i^+ remains as the most stable defect configuration. As shown in Fig. 3c, when changing from compressive to tensile strain, the stable configurations of defects are changed from charged ones to neutral ones, *e.g.*, H_s becomes more stable than H_s^+ and O_v becomes more stable than O_v^+ and O_v^{2+}. Similarly, the formation energy of defects calculated under O-poor conditions is shown in Fig. S4.† At such conditions, the defect configuration is changing from O_v^{2+} to O_v as the strain changes from compression to expansion. However, H_i^+ is still the preferable defect under ambient condition (Fig. S4†). The DOS of anatase with different concentration of H_i^+ compared with pure anatase are shown in Fig. 3d. The energy of doped systems is aligned by shifting 1s state of O atom far away from the defect to that of pure anatase. It can be seen that doping with H_i^+ shifts the valence band edge upwards ($\sim$0.1 eV) without changing the position of the conduction band edge. More specifically, the change of the valence band edge can be explained as the hybridization of 2p states of O atom bonded with H_i^+ and Ti 3d nearby (see Fig. S5†).

Under biaxial strain, due to lattice mismatch, the valence band maximum and conduction band minimum (CBM) of pure anatase (32 atoms supercell) under different strain are calculated and plotted in Fig. 4a. It is clear that both VBM and CBM decrease in energy as strain increases from compressive to tensile strain. When strain increases to 2%, the value of VBM decreases around 0.3 eV. Similarly, the CBM decreases around 0.4 eV. Therefore, the band gap is shrinking as strain increases. When doped with H_i^+, the VBM position is located below the VBM of pure anatase under 2% tensile strain, while the VBM remains unchanged with doped with H_i (shown in Fig. S4†). Hydrogen doping also introduces distortions to anatase TiO_2, which results in the formation of the amorphous TiO_2 at the

interface. To shed further light on this, H doped amorphous TiO_2 was studied with the PBE+U method, keeping the same parameters used for the interface. Doping with H_i is energetically favorable (shown in Fig. S4†) with a formation energy of -0.4 eV for single H_i. The calculated DOS of H doped systems is shown in Fig. 4b. Compared with pure a-TiO_2, single H_i introduces one occupied localized state on top of the valence band edge about 0.5 eV high in energy. The doping with H does not seem to change the averaged electrostatic potential, as can be seen from Fig. S5.† Adding two H_i introduce two localized states in the gap, but with slightly different energies. As more interstitial hydrogens are incorporated, we speculate that these states will eventually form energy levels in the range of up to $\sim$0.7 eV above the valence band edge. These energy levels work as the hole acceptance levels and help the transport of photoexcited holes generated from the Fe_2O_3 side to the H:TiO_2 electrolyte side, where they can take part in the water oxidation reaction.

3.2 Experimental results

To test our hypothesis and to scrutinize the first-principles results experimentally, we have fabricated Fe_2O_3–TiO_2 heterojunction electrodes in two steps. First, we deposited an ultrathin α-Fe_2O_3 (25 nm) film on ITO substrate by thermal evaporation of Fe followed by air annealing at 350 °C. Further, the asprepared α-Fe_2O_3 thin films were coated with TiO_2 by sol–gel spin coating method followed by thermal annealing at 400 °C. In as-prepared Fe_2O_3–TiO_2 heterostructure, the band edge engineering was achieved by hydrogen doping (Fe_2O_3–H:TiO_2) by further annealing the Fe_2O_3–TiO_2 heterostructure in 4% H_2 in Ar at 300 °C at atmospheric pressure for 6 h.

To determine the crystal structures of α-Fe_2O_3, TiO_2, and Fe_2O_3–TiO_2 heterostructure thin films and possible phase changes after hydrogen doping in TiO_2, Raman spectroscopy was performed, and its results are shown in Fig. S7a.† In pristine α-Fe_2O_3, normally seven phonon modes are expected in the Raman spectrum: namely two A_{1g} modes (225 and 498 cm^{-1}) and five E_g modes (247, 293, 299, 412, and 613 cm^{-1}), but the 293 and 299 cm^{-1} bands can only be resolved at temperatures ≤100 K. In the present case, six of the observed bands (A_{1g}, 223 and 498 cm^{-1}; E_g, 244, 294, 410, and 607 cm^{-1}) are detected,
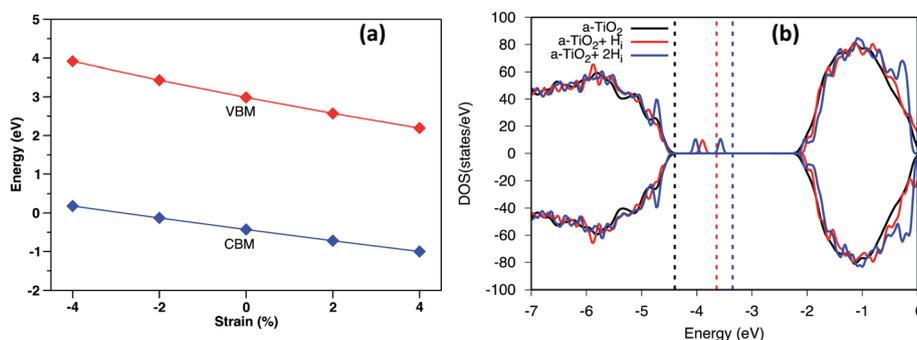

Fig. 4 (a) The calculated VBM and CBM of anatase using HSE06 under different biaxial strain. (b) The DOS of H doped a-TiO_2 compared with pure a-TiO_2. The energy was aligned by the 1s state of O atom far away from the defect. The dashed line indicates the Fermi level of each system.

© 2021 The Author(s). Published by the Royal Society of Chemistry

which agrees with the formation of the hematite phase (α-Fe_2O_3). On the other hand, the Raman spectra of both pristine and hydrogen doped TiO_2 samples exhibit well-resolved TiO_2 Raman peaks at 144 cm^{-1} (E_g), 398 cm^{-1} (B_{1g}), 515 cm^{-1} (E_g), and 640 cm^{-1} (E_g), indicating that anatase is the predominant species, except for 147 cm^{-1} (B_{1g}), which is suppressed by a much stronger E_g peak at 144 cm^{-1}. No phase change after hydrogen doping in TiO_2 was observed (ESI Fig. S7b†). The Raman spectra of TiO_2–Fe_2O_3 heterostructure shows the significant up-shift of E_g mode of TiO_2 from 141 to 155 cm^{-1} and also other bands of TiO_2. The shift of Raman bands by 14 cm^{-1} (inset of ESI Fig. S7b†) is probably due to the strain and defect states at the junction with α-Fe_2O_3 and lattice mismatch. Morphological characteristics were investigated by scanning

electron microscopy (SEM) (ESI Fig. S8†) and transmission electron microscopy (TEM) (ESI Fig. S9†). SEM images of pristine α-Fe_2O_3 electrodes showed uniform deposition of a thin layer of a thickness of about 25 nm without any inter-particle pores, as shown in Fig. S8.† Optimized thickness of TiO_2 layer (thickness < 10 nm) over the α-Fe_2O_3 layer on ITO clearly showed a smooth and dense coverage, as shown in Fig. S8c.†

First, we optimized the temperature for optimized hydrogen doping with respect to the reduction in band gap and upshift of band edge position. Fig. 5a displays the optical absorption spectra of the TiO_2, $H:TiO_2$, samples in the wavelength range 340–600 nm measured by using the integrating sphere. Optical absorption spectra of all the samples, α-Fe_2O_3, TiO_2, $H:TiO_2$, Fe_2O_3–TiO_2, and Fe_2O_3–$H:TiO_2$, in the wavelength range 300–
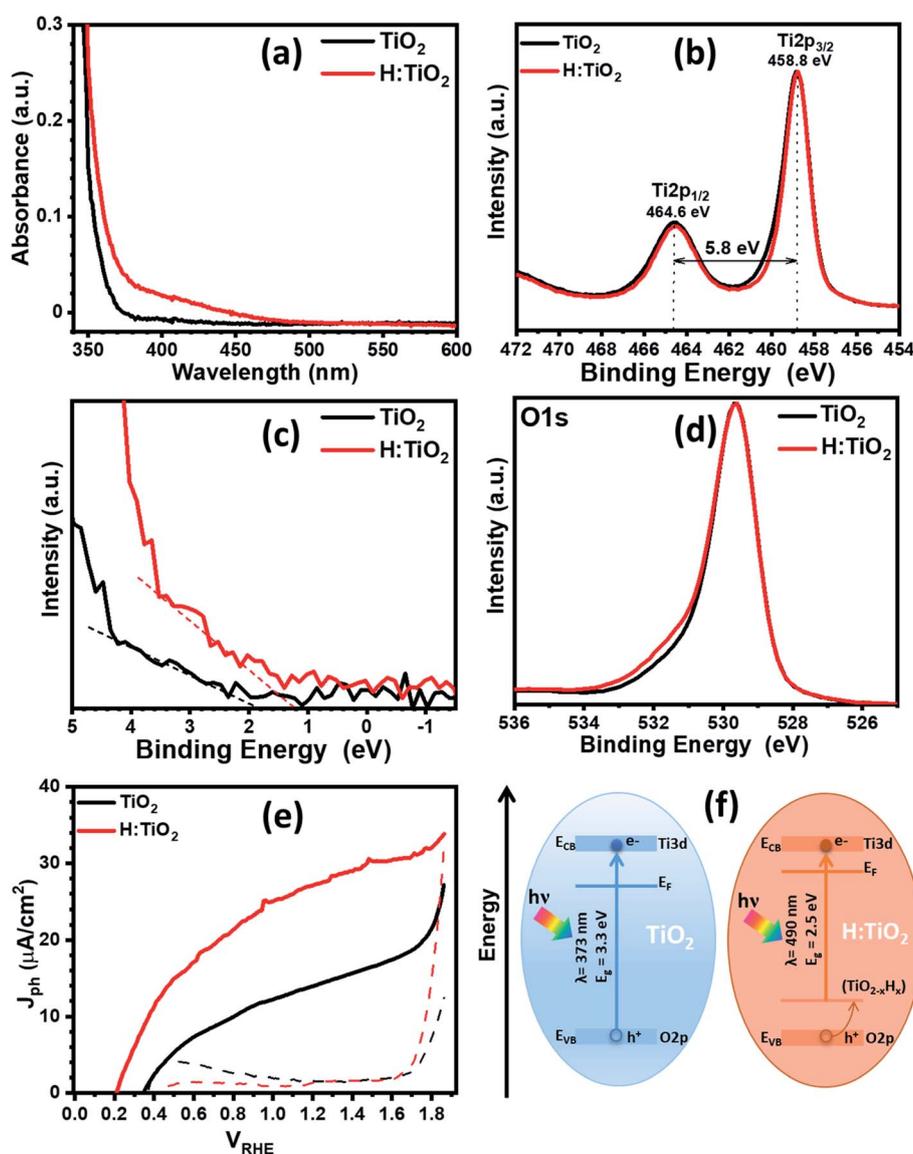

Fig. 5 (a) Optical absorption of pristine and hydrogen treated TiO_2 thin films. (b) Core-level XPS Ti 2p spectra. (c) Valance band spectra of pristine and hydrogen treated TiO_2. (d) Core-level XPS O 1s spectra. (e) Photocurrent density *versus* applied potential for pristine and hydrogen treated TiO_2. (f) Band diagram representation of pristine and hydrogen treated TiO_2. Both representations were built using experimental data from UV-vis spectroscopy and valance band XPS analysis. Conduction band offset was estimated using band gap and valance band offsets.

700 nm measured under the same experimental conditions are shown in the ESI (Fig. S10).† In pristine TiO₂ samples, a steep increase in absorption at wavelengths shorter than ~373 nm can be attributed to the intrinsic band gap of crystalline TiO₂. The hydrogen doping of the TiO₂ sample show a significant shift of absorption edge from higher wavelengths down to 490 nm in the visible light absorption. The calculated values of the band gap energy show that the band gap of the pristine TiO₂ thin films is approximately 3.30 eV, slightly higher than that of bulk anatase TiO₂. However, the onset of light absorption in hydrogen doped TiO₂ thin film is lowered to about 2.5 eV.

To validate the reduction of band gap energy, we have carried out the XPS measurement on both pristine and hydrogen doped TiO₂ thin films to understand the surface chemical bonds, chemical composition, peak position, and hence the electronic properties. Therefore, the Ti 2p, O 1s, and valance band spectra were measured and analyzed for pristine and hydrogen doped TiO₂ thin films. The Ti 2p core level XPS spectrum, Fig. 5b, shows that the Ti 2p$_{3/2}$ peak is at 458.8 ± 0.1 eV, which was attributed to Ti^{4+} states for both the samples. However, after hydrogen doping, a slight asymmetric narrowing in the Ti 2p$_{3/2}$ peak can be seen. This narrowing in the peak upon hydrogen doping is likely due to a decrease in Ti^{3+} states, concurrent with the reduction in oxygen content, and to a disorder due to the thermal annealing of TiO₂ in hydrogen environment.[39] However, no reduction in the Ti^{4+} was observed in TiO₂ after hydrogen doping. Fig. 5c shows the valence band spectra obtained for the pristine and hydrogen treated TiO₂ thin films. The VBM were calculated by linearly extrapolating the peaks to

the baselines. The VBM for pristine TiO₂ thin film was observed at 1.93 eV below the zero potential energy point. However, in the case of hydrogen doped TiO₂ films, VBM was obtained at 1.27 eV. Therefore, a valence band edge shift by ~0.66 eV was observed towards the Fermi level. Moreover, small bands occurred above the VBM, and small bands existed close to the binding energy at zero. In light of the first-principles calculations, the up-shift of the VBM is suggested to be the result of defects states above the valence band induced by interstitial hydrogen in the TiO₂ thin films. Fig. 5d represents the O 1s spectra of pristine and hydrogen doped TiO₂ samples. The peak at a binding energy of 529.6 ± 0.1 eV corresponds to O–Ti bonds in TiO₂ in both the samples. However, in hydrogen doped samples, an additional peak can be seen at 531.6 ± 0.1 eV, which is probably due to oxygen vacancies, formation of hydroxyl groups, and Ti–OH bonds.[39,40] From Fig. S13b and c,† where the XPS spectra of all four samples are shown, it is further visible that Fe₂O₃–H:TiO₂ displays the same narrowing of the Ti^{4+} peak as H:TiO₂, and a more accentuate OH⁻ peak in the oxygen 1s spectrum, correlating the formation of the iron oxide heterostructure with the generation of oxygen vacancies and/or hydroxyl groups.

The PEC measurement in the form of photocurrent densities vs. applied potential (J_{ph} vs. V_{RHE}) curves are shown in Fig. 5e for pristine and hydrogen doped TiO₂ samples under 1 sun illumination. The calculated value of J_{ph} for pristine TiO₂ photoanode was obtained ~14 µA cm⁻² at 1.23 V$_{RHE}$. However, hydrogen doping in TiO₂ enhanced the PEC response significantly and reached a J_{ph} to ~27.4 µA cm⁻² at 1.23 V$_{RHE}$. It is
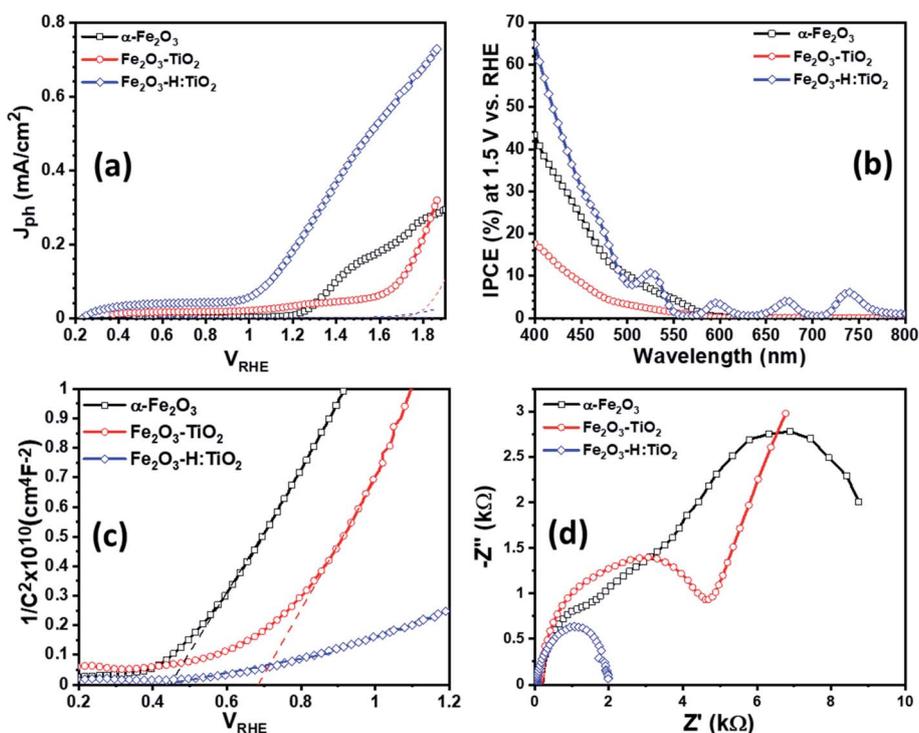

Fig. 6 (a) Photocurrent density versus applied potential (b) IPCE curves measured at 1.5 V vs. RHE for the α-Fe₂O₃, Fe₂O₃–TiO₂, and Fe₂O₃–H:TiO₂ heterostructures photoanodes. (c) Mott–Schottky plots for α-Fe₂O₃, Fe₂O₃–TiO₂, and Fe₂O₃–H:TiO₂ heterostructures measured in 0.1 M NaOH electrolyte solution under 1 sun illumination. (d) Measured EIS Nyquist plots for α-Fe₂O₃, Fe₂O₃–TiO₂ and Fe₂O₃–H:TiO₂ heterostructure.

noticed that hydrogen doping in TiO$_2$ thin films greatly enhanced the J_{ph} and shifted the photocurrent onset potential to 0.2 V$_{RHE}$. The relatively low value of photocurrent onset potential indicates that the charge separation and transportation in hydrogen doped TiO$_2$ thin films are more efficient than the pristine TiO$_2$ thin films. We have also calculated the flat-band potential (V_{fb}) and carrier concentration (N_d) for pristine and hydrogen doped TiO$_2$ samples using Mott–Schottky plots. The value of V_{fb} was calculated from the intercept of the straight line to the x-axis in the linear region of the plot, as shown in Fig. S11.† The pristine TiO$_2$ sample exhibit a V_{fb} value of 0.29 V$_{RHE}$. However, a shift in V_{fb} to 0.15 V$_{RHE}$ was calculated for the H:TiO$_2$ photoanode. This significant shift of V_{fb} by 0.14 V towards the cathodic side in H:TiO$_2$ is likely because the hydrogen doping can enhance the carrier concentration due to increased oxygen vacancies, which could serve as shallow electron donor and upshift the Fermi level towards the conduction band of TiO$_2$. Schematic positions of band edges of TiO$_2$ and H:TiO$_2$ are shown in Fig. 5f. The band alignment of H:TiO$_2$ facilitates more efficient charge separation at the semiconductor/electrolyte interface as compared to pristine TiO$_2$ by increasing the degree of band bending at the H:TiO$_2$ surface. The experimental value of V_{fb} for H:TiO$_2$ is more cathodic in comparison to the pristine TiO$_2$, which favors the water splitting reaction. In summary, the enhancement in photocurrent density in the H:TiO$_2$ sample is thanks to the combined effect of decreased bandgap energy, which allows absorption of a wide range of solar radiation, high donor density which is responsible for the shift in Fermi level towards the conduction band, and more negative flat band potential.

To examine the PEC performance of the targeted heterostructures photoanodes, Fe$_2$O$_3$–TiO$_2$ and Fe$_2$O$_3$–H:TiO$_2$, the J_{ph} vs. V_{RHE} characteristics under dark and illumination was measured in a three-electrode PEC cell. Fig. 6a depicts the PEC performance of the optimized Fe$_2$O$_3$–TiO$_2$ and Fe$_2$O$_3$–H:TiO$_2$ heterostructures compared with pristine α-Fe$_2$O$_3$ photoanode. The dark current densities, for the applied potential range up to 1.7 V$_{RHE}$, are negligible for all samples. The J_{ph} of the pure α-Fe$_2$O$_3$ photoanode is ~10 μA cm^{-2} at 1.23 V vs. RHE, which is reasonable as compared to the previously reported values due to the difference in the film thickness and has an onset of photocurrent at 1.15 V$_{RHE}$.[20] A much lower onset potential of ~0.35 V$_{RHE}$ and lower J_{ph} of ~35 μA cm^{-2} at 1.23 V$_{RHE}$ obtained for the Fe$_2$O$_3$–TiO$_2$ heterostructure. However, the hydrogen doped TiO$_2$ layer in the Fe$_2$O$_3$–H:TiO$_2$ heterostructure substantially shifted the onset of photocurrent to 0.21 V$_{RHE}$ and the J_{ph} at 1.23 V$_{RHE}$ increased to 215 μA cm^{-2}. The value of J_{ph} for Fe$_2$O$_3$–H:TiO$_2$ heterostructure photoanode reached 450 μA cm^{-2} at 1.5 V$_{RHE}$, which is three and nine times the J_{ph} for α-Fe$_2$O$_3$ (153 μA cm^{-2}) and Fe$_2$O$_3$–TiO$_2$ (51 μA cm^{-2}) photoanodes, respectively. The obtained value of J_{ph} for Fe$_2$O$_3$–H:TiO$_2$ heterostructured system is significantly high to that of a pristine α-Fe$_2$O$_3$ and Fe$_2$O$_3$–TiO$_2$ systems. As the magnitude of J_{ph} corresponds to the number of photogenerated holes that reach the electrode surface, the Fe$_2$O$_3$–TiO$_2$ sample exhibits a high recombination of photogenerated electrode and holes at the junction due to the discontinuity of the mismatch of band edge

positions, which hinders the water oxidation process at the surface of the Fe$_2$O$_3$–TiO$_2$ photoanode. As we reported in our previous work on hydrogen treated TiO$_2$ and predicted in our simulation for this work, hydrogen doping in TiO$_2$ can upshift the valance band position and create the lattice defects in TiO$_2$. Our simulation results on hydrogen doping in TiO$_2$ indicate that heterojunctions of α-Fe$_2$O$_3$ and hydrogen doped TiO$_2$ can lead to considerably enhanced hole transport from α-Fe$_2$O$_3$ to H:TiO$_2$ and, thus, to a more efficient separation of photoexcited electron–hole pairs. Consequently, hydrogen treated Fe$_2$O$_3$–TiO$_2$ photoanode exhibits a higher number of photogenerated holes that can participate in the oxidation process before recombining with excited electrons.

Further, to quantitatively investigate the PEC performance of the photoanodes, incident photon-to-current conversion efficiency (IPCE) measurements were performed at 1.5 V vs. RHE in 1.0 M KOH and shown in Fig. 6b. All the samples show photocurrent response to incident light in the wavelength region of 400–580 nm, which matches the bandgap of hematite (~2.1 eV). The pristine α-Fe$_2$O$_3$ photoanode exhibits 42% IPCE at the excitation wavelength of 400 nm, which is comparable with the reported IPCE values of α-Fe$_2$O$_3$ photoanode. A significantly low IPCE, 18%, was recorded in the case of the Fe$_2$O$_3$–TiO$_2$ photoanode. This Fe$_2$O$_3$–TiO$_2$ photoanode also exhibits the low photocurrent density in PEC measurements. However, Fe$_2$O$_3$–H:TiO$_2$ photoanode exhibits substantially high quantum efficiency as compared with pristine α-Fe$_2$O$_3$ and Fe$_2$O$_3$–TiO$_2$ photoanodes in the wavelength range of 400–550 nm. The IPCE of the Fe$_2$O$_3$–H:TiO$_2$ photoanode reaches to ~65% at the excitation wavelength of 400 nm, which is 1.5 and 3.6 times that of α-Fe$_2$O$_3$ (42%) and Fe$_2$O$_3$–TiO$_2$ (18%), respectively.

To gain even more insight into the enhancement of photocurrent density and IPCE values in Fe$_2$O$_3$–H:TiO$_2$ heterostructure photoanodes, Mott–Schottky measurements were performed with applied potential at 1 kHz frequency in the dark. From the Mott–Schottky plots, which represent the changes in capacitance (C) against the applied potential, it can be seen that all the samples possess a positive slope (Fig. 6c), which is a characteristic of n-type semiconductors with electrons as majority carriers. The flat band potential (V_{fb}) and carrier density (N_d) were calculated from the slopes of Mott–Schottky plots. The value of V_{fb} was observed to shift towards the more cathodic side from 0.44 V$_{RHE}$ for α-Fe$_2$O$_3$ to 0.68 V$_{RHE}$ for the Fe$_2$O$_3$–TiO$_2$ sample. However, after the hydrogen treatment of the TiO$_2$ layer, the flat band potential remains at the same values to 0.28 V$_{RHE}$ as Fe$_2$O$_3$–TiO$_2$.

Further, the charge transport properties of the Fe$_2$O$_3$–TiO$_2$ and Fe$_2$O$_3$–H:TiO$_2$ photoanodes were investigated by electrochemical impedance spectroscopic (EIS) measurements at 1.23 V$_{RHE}$ applied potential under one sun illumination conditions and compared with α-Fe$_2$O$_3$. Fig. 6d shows the EIS Nyquist plots for α-Fe$_2$O$_3$, Fe$_2$O$_3$–TiO$_2$, and Fe$_2$O$_3$–H:TiO$_2$ photoanodes. The series resistance (R_s) at the interface between the ITO substrate and α-Fe$_2$O$_3$ and Fe$_2$O$_3$–TiO$_2$ layers display a substantial reduction from ca. 140 Ω cm^{-2} for the pristine α-Fe$_2$O$_3$ sample, to 120 Ω cm^{-2} for Fe$_2$O$_3$–TiO$_2$, to ca. 40 Ω cm^{-2} for the Fe$_2$O$_3$–H:TiO$_2$ photoanode surface. The radii of the semicircle in the

EIS plots from the Fe_2O_3–H:TiO_2 heterostructure is much smaller than that from Fe_2O_3–TiO_2, which indicates that the hydrogen treatment of the TiO_2 layer changes the charge distribution in Fe_2O_3–H:TiO_2. The new charge distribution results in a lower magnitude of the equivalent series resistance in Fe_2O_3–H:TiO_2 heterojunction photoanodes indicating strongly improved charge transport properties as compared to Fe_2O_3–H:TiO_2.

Finally, in order to assess the durability of the photoanodes, chronoamperometry was performed on the Fe_2O_3–TiO_2 and the Fe_2O_3–H:TiO_2 electrodes (as presented in Fig. S12 in the ESI†): the resulting photocurrent density, under a bias voltage of 0.5 V_{RHE} and an illumination of 1 sun, was found to be stable around a value of 0.4 mA cm^{-2} for up to 500 minutes for Fe_2O_3–H:TiO_2, with no sign of decreasing, while the non-treated sample displayed a lower photocurrent (0.23 mA cm^{-2}) at the start, which halved after less than 300 minutes of continuous use. This sustained stability of Fe_2O_3–H:TiO_2 electrodes confirms the applicability of the device.

4. Conclusion

First-principles calculations predict that hydrogen treatment induce states above the valance band, which can transfer holes through the heterostructure junction. The predictions are validated with experimental observation obtained on sol–gel grown TiO_2 thin films. Optical absorption, XPS analysis, and (photo) electrochemical measurements show that the tailoring in optical band gap, shift in valence band position, and change in electrical properties in hydrogen doped TiO_2 results in a type II band alignment in the Fe_2O_3–H:TiO_2 heterostructure. The Fe_2O_3–H:TiO_2 heterostructure reduces the electron–hole recombination sharply at the junction and improves the water oxidation performance. This study shows that hydrogen treatment can enhance the photoelectrochemical response of the Fe_2O_3–TiO_2 heterostructure, thanks to the formation of type II band alignment at the interface junction. The theoretical and experimental strategies can be applied to other oxides based heterostructures and might become important tools for engineering efficient and stable photoelectrodes.

Author contributions

A. P. S., B. W. and A. H. conceived the idea and designed the experimental work. A. H. and R. B. W. supported the work through theoretical simulations. A. P. S. have prepared and characterized the samples for experimental work and R. B. W. preformed the thermotical simulation. A. P. S., B. W. and A. H. analyzed the experimental data for the manuscript. The manuscript was written through the contributions of all authors. All authors have given approval to the final version of the manuscript.

Conflicts of interest

There are no conflicts to declare.

Acknowledgements

References

1 M. Grätzel, *Nature*, 2001, **414**, 338–344.
2 H. Ahmad, S. K. Kamarudin, L. J. Minggu and M. Kassim, *Renewable Sustainable Energy Rev.*, 2015, **43**, 599–610.
3 Y. Tachibana, L. Vayssieres and J. R. Durrant, *Nat. Photonics*, 2012, **6**, 511–518.
4 A. Fujishima and K. Honda, *Nature*, 1972, **238**, 37–38.
5 A. Fujishima, T. N. Rao and D. A. Tryk, *J. Photochem. Photobiol., C*, 2000, **1**, 1–21.
6 A. P. Singh, S. Kumari, R. Shrivastav, S. Dass and V. R. Satsangi, *Int. J. Hydrogen Energy*, 2008, **33**, 5363–5368.
7 M. R. Hoffmann, S. T. Martin, W. Choi and D. W. Bahnemann, *Chem. Rev.*, 1995, **95**, 69–96.
8 M. Mehta, N. Kodan, S. Kumar, A. Kaushal, L. Mayrhofer, M. Walter, M. Moseler, A. Dey, S. Krishnamurthy, S. Basu and A. P. Singh, *J. Mater. Chem. A*, 2016, **4**, 2670–2681.
9 A. P. Singh, N. Kodan and B. R. Mehta, *Appl. Surf. Sci.*, 2016, **372**, 63–69.
10 A. P. Singh, N. Saini and B. R. Mehta, *ChemistrySelect*, 2017, **2**, 1413–1420.
11 A. P. Singh, A. Mettenbörger, P. Golus and S. Mathur, *Int. J. Hydrogen Energy*, 2012, **37**, 13983–13988.
12 S. Shen, S. A. Lindley, X. Chena and J. Z. Zhang, *Energy Environ. Sci.*, 2016, **9**, 2744–2775.
13 L. Pei, H. Wang, X. Wang, Z. Xu, S. Yan and Z. Zou, *Dalton Trans.*, 2018, **47**, 8949–8955.
14 S. Choudhary, S. Upadhyay, P. Kumar, N. Singh, V. R. Satsangi, R. Shrivastav and S. Dass, *Int. J. Hydrogen Energy*, 2012, **37**, 18713–18730.
15 D. Barreca, G. Carraro, A. Gasparotto, C. Maccato, M. E. A. Warwick, K. Kaunisto, C. Sada, S. Turner, Y. Gönüllü, T. -P. Ruoko, L. Borgese, E. Bontempi, G. V. Tendeloo, H. Lemmetyinen and S. Mathur, *Adv. Mater. Interfaces*, 2015, **2**, 1500313.
16 R. d. S. Santos, G. A. Faria, C. Giles, C. A. P. Leite, H. d. S. Barbosa, M. A. Z. Arruda and C. Longo, *ACS Appl. Mater. Interfaces*, 2012, **4**, 5555–5561.
17 A. P. Singh, N. Kodan, B. R. Mehta, A. Held, L. Mayrhofer and M. Moseler, *ACS Catal.*, 2016, **6**, 5311–5318.
18 M. A. Butler and D. S. Ginley, *J. Electrochem. Soc.*, 1978, **125**, 228–232.
19 A. P. Singh, N. Kodan, B. R. Mehta, A. Dey and S. Krishnamurthy, *Mater. Res. Bull.*, 2016, **76**, 284–291.

20 A. P. Singh, A. Levinsson, B. Iandolo, J. Oksanen, A. Hellman and B. Wickman, *J. Photochem. Photobiol., A*, 2020, **401**, 112781.

21 G. Kresse and J. Hafner, *Phys. Rev. B: Condens. Matter Mater. Phys.*, 1993, **47**, 558–561.

22 G. Kresse and D. Joubert, *Phys. Rev. B: Condens. Matter Mater. Phys.*, 1999, **59**, 1758–1775.

23 G. Kresse and J. Furthmüller, *Phys. Rev. B: Condens. Matter Mater. Phys.*, 1996, **54**, 11169–11186.

24 P. E. Blöchl, *Phys. Rev. B: Condens. Matter Mater. Phys.*, 1994, **50**, 17953–17979.

25 J. P. Perdew, J. A. Chevary, S. H. Vosko, K. A. Jackson, M. R. Pederson, D. J. Singh and C. Fiolhais, *Phys. Rev. B: Condens. Matter Mater. Phys.*, 1992, **46**, 6671–6687.

26 S. L. Dudarev, G. A. Botton, S. Y. Savrasov, C. J. Humphreys and A. P. Sutton, *Phys. Rev. B: Condens. Matter Mater. Phys.*, 1998, **57**, 1505–1509.

27 B. J. Morgan and G. W. Watson, *Phys. Rev. B: Condens. Matter Mater. Phys.*, 2010, **82**, 144119.

28 Z. Hu and H. Metiu, *J. Phys. Chem. C*, 2011, **115**, 5841–5845.

29 J. Heyd, G. E. Scuseria and M. Ernzerhof, *J. Chem. Phys.*, 2003, **118**, 8207–8215.

30 J. Heyd and G. E. Scuseria, *J. Chem. Phys.*, 2004, **121**, 1187–1192.

31 H. J. Monkhorst and J. D. Pack, *Phys. Rev. B: Solid State*, 1976, **13**, 5188–5192.

32 L. Kleinman, *Phys. Rev. B: Condens. Matter Mater. Phys.*, 1981, **24**, 7412–7414.

33 D. M. Bylander and L. Kleinman, *Phys. Rev. B: Condens. Matter Mater. Phys.*, 1987, **36**, 3229–3236.

34 C. G. Van de Walle, *Phys. Rev. B: Condens. Matter Mater. Phys.*, 1989, **39**, 1871–1883.

35 M. Peressi, N. Binggeli and A. Baldereschi, *J. Phys. D: Appl. Phys.*, 1998, **31**, 1273–1299.

36 A. Baldereschi, S. Baroni and R. Resta, *Phys. Rev. Lett.*, 1988, **61**, 734–737.

37 X. Luo, G. Bersuker and A. A. Demkov, *Phys. Rev. B: Condens. Matter Mater. Phys.*, 2011, **84**, 195309.

38 B. Iandolo, B. Wickman, E. Svensson, D. Paulsson and A. Hellman, *Nano Lett.*, 2016, **16**, 2381–2386.

39 B. Bharti, S. Kumar, H.-N. Lee and R. Kumar, *Sci. Rep.*, 2016, **6**, 32355.

40 A. P. Singh, C. Tossi, I. Tittonen, A. Hellman and B. Wickman, *RSC Adv.*, 2020, **10**, 33307–33316.